Development of a Two-Channel Aerosol Retrieval Algorithm on a Global Scale Using NOAA AVHRR

AKIKO HIGURASHI AND TERUYUKI NAKAJIMA

Center for Climate System Research, University of Tokyo, Tokyo, Japan

(Manuscript received 22 May 1997, in final form 9 June 1998)

ABSTRACT

This study proposes a two-channel satellite remote sensing algorithm for retrieving the aerosol optical thickness and the Ångström exponent, which is an index for the aerosol size distribution. An efficient lookup table method is adopted in this algorithm to generate spectral radiances in channels 1 and 2 of National Oceanic and Atmospheric Administration (NOAA) Advanced Very High Resolution Radiometer (AVHRR) over ocean areas. Ten-day composite maps of the aerosol optical thickness and the Ångström exponent have been obtained from AVHRR global area coverage data in January and July of 1988. Aerosol optical thickness maps show that the major aerosol sources are located off the west coast of northern and southern Africa, and the Arabian Peninsula. The most important contributor is soil-derived particles from the Sahara Desert that cross the Atlantic Ocean. The authors' optical thickness values tend to be larger than values given by the NOAA operational algorithm. A 10-day composite map of Ångström exponent showing man-made air polluted regions, such as the Mediterranean Sea, the Black Sea, and the east coasts of North America and China, has large values, suggesting that small particles are dominant in these regions.

1. Introduction

The impact of atmospheric aerosols on the earth's climate has been recognized as an important problem for understanding the climate formation, especially after several studies have pointed out that aerosols are the source of the greatest uncertainties in evaluating climate forcing (Hansen and Lacis 1990; Shi et al. 1994). Aerosols directly influence the climate through perturbation of the radiation budget by scattering solar radiations back to space (leading to negative radiative forcing) and by absorbing solar and thermal radiations (leading to positive forcing). Acting as cloud condensation nuclei or ice nuclei, aerosol particles modify the cloud microphysics (Twomey 1977; Kaufman and Nakajima 1993), and hence, aerosol particles also indirectly have an effect on climate. In contrast to the greenhouse gases, which act only on the longwave radiation process, aerosol particles can influence both shortwave and longwave radiation. The magnitude of the effects also depends on their composition and size.

Radiative forcing of sulfate aerosols has been studied extensively by many investigators with a recognition that they are climatologically most important for evaluating the anthropogenic global warming trend. Their globally averaged direct effect is estimated as -0.3 to -0.9 W m^{-2} (Charlson et al. 1992; Kiehl and Briegleb 1993; Taylor and Penner 1994), and the indirect effect is about -1.3 W m^{-2} (Jones et al. 1994). These studies suggest, therefore, that total sulfate aerosol forcing is comparable in magnitude to the current anthropogenic greenhouse gas forcing but in opposite sign. There is, however, a large uncertainty in the evaluation of both direct and indirect effects of the sulfate aerosols. The forcing mechanism with aerosols is highly complex and needs more study before drawing a clear *conclusion*. For example, aerosols originated from dimethyl sulfate (DMS) may change cloud microphysics significantly. Such indirect effects will be temperature dependent and, hence, may make a feedback loop with the global warming process. Some studies have suggested recently that mineral dust aerosols generated from disturbed soil are important as a climate forcing agent that needs to be included among the climate forcing factors influenced by human activities (Li et al. 1996; Tegen et al. 1996).

In order to reduce the above-mentioned large uncertainties in evaluation of the aerosol forcing, it is necessary to improve our knowledge of aerosol characteristics, such as the total content, composition, etc., on a global scale. A use of satellites is very effective to study aerosol optical properties on a large scale. So far, most of the aerosol remote sensing studies have been made using National Oceanic and Atmospheric Administra-

Corresponding author address: Teruyuki Nakajima, Center for Climate System Research, University of Tokyo, 4-6-1 Komaba, Meguro-ku, Tokyo, 153, Japan.
E-mail: teruyuki@ccsr.u-tokyo.ac.jp

tion (NOAA)/Advanced Very High Resolution Radiometer (AVHRR) channel 1 and/or 2. Stowe et al. (1992) produced global maps of the aerosol optical thickness at wavelength of 0.5 μm over ocean area using channel-1 radiances of AVHRR. Although the one-channel algorithm is appreciated for showing the global distribution of the aerosol optical thickness, there is some tendency toward underestimation of the optical thickness due to the assumed aerosol particle size distribution and refractive index as shown by Ignatov et al. (1995a) and Ignatov et al. (1995b). Durkee et al. (1992) pointed out the importance of the impact of the phase function assumed in the one-channel algorithm and introduced a two-term Henyey–Greenstein phase function to solve this problem. They obtained a global map of an index of size distribution, which is the ratio of channel-1 and -2 radiances of AVHRR, in addition to the optical thickness obtained from channel-1 radiance. To simplify the problem, they adopted the single-scattering approximation in the transfer calculation of their algorithm. Such an approximation is, however, questionable for thick absorbing aerosol cases such as Saharan desert aerosols. Moreover, they did not report how to treat water vapor absorption in channel 2 of AVHRR, which significantly affects the channel-2 radiance (Stowe et al. 1997). Kaufman et al. (1990) proposed an algorithm to estimate the aerosol optical thickness, the particle geometrical mean mass radius, and the single scattering albedo from channels 1 and 2 of AVHRR. Nakajima and Higurashi (1997) retrieved aerosol optical thickness, Ångström exponent, and single-scattering albedo of aerosols for the Persian Gulf oil fire event in 1991 by a method similar to Kaufman et al. (1990). Those two algorithms are significant for improving the aerosol remote sensing, because it is possible to retrieve almost all important parameters to describe the aerosol optical properties over land and ocean. Their applications are, on the other hand, limited to local area data analyses so far, and extension to global analyses is not so trivial because of the complexity involved in the algorithms. For example, global analyses need to take into account the effects of geophysical parameters, such as water vapor profile, ozone amount, and surface wind velocity, which are fixed in the regional analyses but are variable on a global scale. Also, the algorithm using a reflectance contrast of images between clear and hazy days has to find an automatic detection algorithm of the contrast.

In this paper, we propose a two-channel algorithm for retrieving aerosol optical characteristics from AVHRR channel-1 and -2 radiances that is simple and efficient enough for global-scale analyses. For this purpose we reinvestigate the structure of the radiance field in aerosol-loaded atmosphere–ocean systems in section 2. With these analyses, we will propose an efficient lookup table method to synthesize satellite-received radiances accurately and efficiently with careful correction of multiple scattering and gaseous absorption in channel-1 and -2 radiances. The proposed algorithm will be tested by extensive numerical simulations as shown in section 3. Finally it will be applied to real AVHRR global area coverage (GAC) data in January and August of 1988 for generating global aerosol maps.

2. Radiance fields in aerosol-loaded atmosphere–ocean systems

The satellite-received shortwave radiance emerges from an atmosphere–ocean system as a result of interaction with atmosphere, ocean surface, and ocean body. It is important to study the dependence of the radiance on inherent parameters describing the optical properties of the atmosphere–ocean system in order to develop a lookup table (LUT) approach, which is efficient for global remote sensing analyses.

a. The structure of radiance fields

The satellite signal over ocean area is composed of contributions from atmospheric path radiance and water-leaving radiance. The water-leaving radiance is further composed of reflection by the ocean surface, scattering by foams, and upwelling radiance from the ocean body. The latter two components can be ignored for most applications at wavelengths of AVHRR channels 1 and 2 (λ = 0.64 and 0.83 μm) due to large water absorption.

The traditional method of the atmospheric correction (Gordon and Wang 1992) introduces a linearized single scattering approximation, R_{as}, to synthesize the apparent reflectance R detected by a satellite radiometer as

$$R \approx R_{as} + R_{mol} + R_g, \tag{1}$$

where R_{mol} and R_g are apparent reflectances for the molecular atmosphere without aerosol loading and for sunglint component, respectively. We define the apparent reflectance as

$$R = \frac{\pi L}{\mu_0 F_0}, \tag{2}$$

with the satellite-received radiance L, the extraterrestrial solar incident flux F_0, and the cosine of solar zenith angles, $\mu_0 = \cos\theta_0$. The linearized aerosol single scattering component is expressed as

$$R_{as} = \frac{\pi \omega_a P_a(\Theta)}{\mu\mu_0} \tau_a, \tag{3}$$

where ω_a, τ_a, and $P_a(\Theta)$ are the aerosol single-scattering albedo, optical thickness, and phase function, respectively; and μ is the cosine of zenith angle of the emergent radiation, θ. Equation (1), with Eq. (3), has a large error in the synthesized reflectance for large optical thickness and/or absorbing aerosol cases.

Trying to improve the approximation, Wang and Gordon (1993) have found that the multiple aerosol–molecular scattering component is almost proportional to

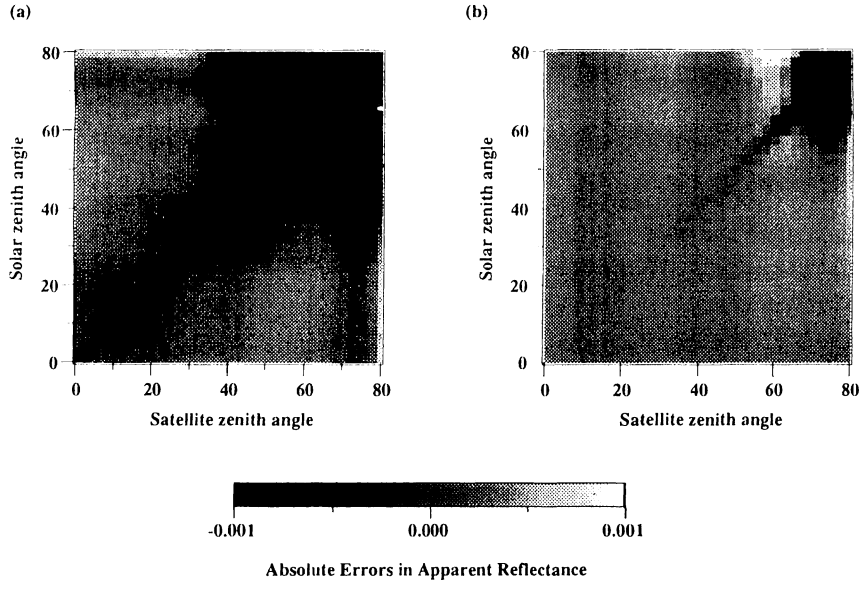

FIG. 1. (a) Absolute errors in the apparent reflectance at the TOA synthesized by Eq. (5) for various solar and satellite zenith angles: $\tau_a = 0.1$; (b) Same as (a), but synthesized by Eq. (9).

the linearized aerosol single-scattering reflectance as follows:

$$R - R_{\text{mol}} - R_g = \sum_{n=0}^{2} c_n R_{\text{as}}^n. \tag{4}$$

They successfully reduced the error involved in synthesized radiances with Eq. (4). Introducing Eq. (3) into Eq. (4), we have the following expression for the multiple aerosol-molecular scattering component:

$$R - R_{\text{mol}} - R_{\text{as}} - R_g = \frac{1}{\mu\mu_0} \sum_{n=0}^{2} c_n \tau_a^n. \tag{5}$$

This formula is in some sense more convenient for retrieving the aerosol optical thickness τ_a than using Eq. (4), since Eq. (5) is in a form of series expansion of τ_a. Also, it should be noted that it is not suitable to expand the multiple-scattering component, which is a weak function of angular variables, by the linearized single scattering component R_{as}, which is a strong function of angular variables with the aerosol phase function $P(\Theta)$. On the other hand, this part is suitably separated in Eq. (5) by R_{as} in the left-hand side of the equation. The Advanced Earth Observing Satellite (ADEOS) Ocean Color and Temperature Scanner (OCTS) operational algorithm has adopted this formula (Nakajima and Fukushima 1996).

Although the approximations in Eqs. (4) and (5) will be accurate enough for most applications, one can find large errors exceeding 0.1% at large zenith angles as well as at sun-glint angles as shown in Fig. 1a, which indicates absolute errors in apparent reflectances for various solar and satellite zenith angles at the azimuth angle of 0° and at the aerosol optical thickness of 0.1. In the figure the exact values have been calculated by a general radiative transfer code for atmosphere–ocean–land system, Rstar-5b, which is developed by the Center for Climate System Research (CCSR), University of Tokyo. This code accounts for multiple scattering in the atmosphere by molecules and aerosol particles and bidirectional surface reflection (Nakajima and Tanaka 1986, 1988). The ocean surface reflection is calculated using a rough ocean model (Nakajima and Tanaka 1983). The gaseous absorption is taken into account with the Lowtran-7 absorption model (Kneizys et al. 1988). In this experiment, we assumed the U.S. standard atmosphere and the lognormal volume spectrum for aerosol size distribution as

$$\frac{dV}{d\ln r} = C \exp\left[-\frac{1}{2}\left(\frac{\ln r - \ln r_m}{\ln s}\right)^2\right], \tag{6}$$

where V is the aerosol volume density, r_m is the mode radius in μm, and $\ln(s)$ is the standard deviation of $\ln(r)$. Here, r_m and s are set to 0.2 and 1.5, respectively. As shown by Fig. 1a, large errors appear at large angles as well as in sun-glint region. Numerical simulations have shown that these large errors are caused by the linearized single-scattering approximation (3) adopted in (5), which is not suitable at such large zenith angles.

The above observation in Fig. 1a makes us think about an exact solution for single scattering (Chandrasekhar 1960) for synthesizing the satellite-received reflectance:

$$R_s = \frac{\pi\omega P(\Theta)}{\mu\mu_0 F_0} \frac{1 - \exp[-\tau(1/\mu + 1/\mu_0)]}{1/\mu + 1/\mu_0}, \tag{7}$$

where ω, τ, and $P(\Theta)$ are the single-scattering albedo, optical thickness, and phase function of the atmospheric layer, respectively. In the actual coding we have taken

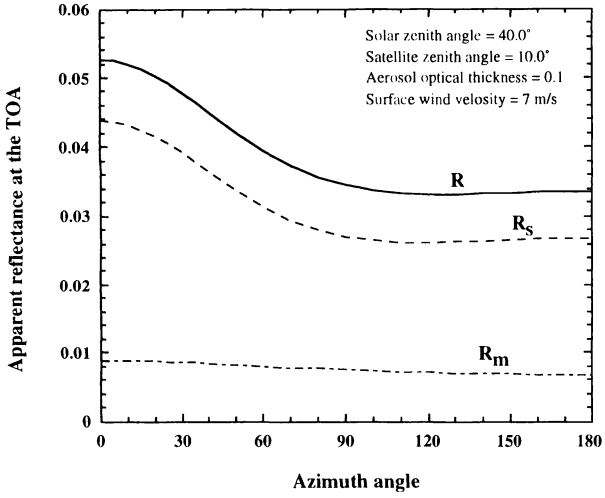

FIG. 2. The angular dependence of the apparent reflectance at TOA for single-scattering component R_s, multiple scattering components R_m, and total value R.

into account the inhomogenity of the atmosphere by setting multilayers (Nakajima and Tanaka 1988). With the definition of Eq. (7), we have the following expression for the apparent reflectance at the top of the atmosphere (TOA) into single- and multiple-scattering contributions:

$$R = R_s + R_m. \tag{8}$$

Figure 2 shows each component in Eq. (8) as a function of the azimuth angle. It is found from Fig. 2 that the large angle dependence in the reflectance is caused by the single scattering component, and hence it is effective to tabulate the multiple scattering component for making the LUT. Some further consideration and numerical tests have suggested that tabulation of the coefficients in the following expansion is more effective than using Eq. (5):

$$R - R_s - R_g = \frac{1}{\mu\mu_0}\left\{\sum_{n=0}^{3} c_n \tau_a^n + c_4 \exp\left[-\tau_a\left(\frac{1}{\mu} + \frac{1}{\mu_0}\right)\right]\right\}. \tag{9}$$

The exponent term in the right-hand side of Eq. (9) is introduced to take into account the fact suggested by Gordon and Wang (1993), that is, the multiple-scattering component has a similar optical thickness dependence to the linearized single-scattering approximation (3), even though the exact single scattering (7) has an exponential function dependence. The cubic polynomial expansion is also introduced to improve the approximation for large optical thickness cases. Figure 1b shows that the approximation with Eq. (9) is much better than with Eq. (5), shown in Fig. 1a, especially for larger zenith angle cases. Detailed investigation (Higurashi et al. 1999, manuscript submitted to *Appl. Opt.*) has found that the exponential term in both sides of Eq. (9) is needed to improved the approximation.

b. Optical models of aerosols

A suitable assumption of the aerosol optical model is another important point for realizing a good aerosol retrieval algorithm, since the inversion is not unique for retrieving the parameters to model the aerosol optical properties. With two wavelengths in our situation, a reasonable strategy will be to assume a suitable size distribution that is applicable enough for various conditions and simple enough to have a small number of parameters to model the aerosol size distribution.

Aerosol size distributions have been measured under various conditions since the early 1970s. Junge (1969) and Toon and Pollack (1976) proposed that a power-law size distribution is representative for stratospheric and tropospheric aerosols. Whitby (1978) showed that a multimode lognormal size distribution is observed for atmospheric aerosols generated by different physical processes. He introduced three modes: 1) the nucleation mode, which is produced by gas-to-particle conversion; 2) the accumulation mode by coagulation and heterogeneous condensation, and 3) the coarse mode originating from the earth's surface. Patterson and Gillette (1977) confirmed that the common feature of the aerosol size distribution is a multimode lognormal size distribution. Although the power-law size distribution certainly represents the general features of aerosols, bimodal or trimodal lognormal size distributions will be more general in describing the optical properties of aerosols if we put more emphasis on inversion results of optical remote sensing data, such as those of Kondratyev et al. (1981), Nakajima et al. (1989), Shiobara et al. (1991), Kaufman et al. (1994), Remer et al. (1997), etc. Those optically equivalent size distributions have common features such as a saddle point around 0.6 μm reflecting in situ measured size distributions. Most of the features of phase functions and optical thickness spectra can be simulated by bimodal functions, rather than by power-law functions.

With the above-mentioned rationale, we introduce in this study a bimodal lognormal volume spectrum for modeling the aerosol size distribution,

$$\frac{dV}{d\ln r} = \sum_{n=1}^{2} C_n \exp\left[-\frac{1}{2}\left(\frac{\ln r - \ln r_{mn}}{\ln s_n}\right)^2\right], \tag{10}$$

where subscript n indicates the mode number. Table 1 lists r_{mn} and s_n of measured volume spectra for nth mode. Averaging the tabulated values, we adopt $r_{m1} = 0.17$ μm, $r_{m2} = 3.44$ μm, $s_1 = 1.96$, and $s_2 = 2.37$ for the parameters of the modeled volume spectrum in our retrieving scheme. Two undetermined parameters in Eq. (10), c_1 and c_2, can be determined from two-channel satellite radiances. Equivalently, we determine the aerosol optical thickness and the peak ratio of the bimodal

TABLE 1. Parameters for the aerosol size distribution fitted to two term lognormal functions.

Reference	r_{m1}	s_1	r_{m2}	s_2	r_{m3}	σ_3	Notes
Patterson and Gillete 1977	0.14	1.56	2.29	2.11			light aerosol loading
			2.84	1.90	35.5	1.38	moderate
			3.08	2.20	35.1	1.37	heavy
Fujimura and Hashimoto 1977	0.41	1.36	2.3	1.65			at Morioka, in winter
	0.36	1.58					at Yokohama
Slinn 1983	0.17	1.61					continental background
	0.19	1.64					urban pollutant
Tanaka et al. 1983	0.14	2.6					yearly averaged
Fitch and Cress 1981	—	1.5					
Nakajima et al. 1986	0.13	1.8			10.0	2.6	
Shiobara et al. 1991	0.16	1.79	4.48	3.47			winter in Sendai
	0.17	1.69	2.78	3.06			spring in Sendai
	0.21	1.97	2.98	2.17			summer in Sendai
	0.15	1.96	3.96	3.12			autumn in Sendai
Whitby 1975	0.17	2.05	4.375	2.33	(0.0215	0.74)	$m = 1.5 - 0.006i$
Nilsson 1979	0.175	2.34	3.41	2.23			
	0.205	2.23	4.09	2.23			
	0.189	2.12	3.41	2.23			
	0.174	2.01	4.09	2.23			
	0.196	2.01	4.09	2.23			

size distribution, $\gamma\ (=c_2/c_1)$. It should be noted that the peak ratio γ, which represents the contribution of large particles, can be related to the Ångström exponent α defined as

$$\alpha = -\frac{d \ln \tau_{a\lambda}}{d \ln \lambda}. \tag{11}$$

The Ångström exponent α is approximately constant in visible spectral region since the optical thickness spectrum is approximately a power-law function of λ for most of observed size distributions as many investigators have pointed out. Defining the mean Ångström exponent α for regular sun-photometer wavelengths,

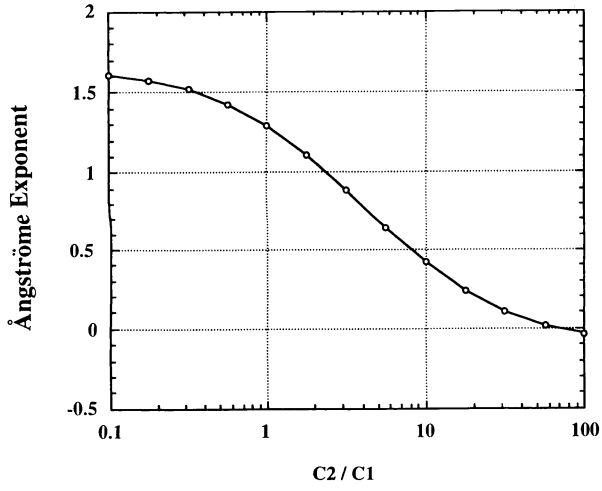

FIG. 3. The relationship between Ångström exponents and peak ratios of bimodal size distributions.

0.368, 0.500, 0.675, 0.862, and 1.050 μm, the peak ratio γ can be translated to α as shown by Fig. 3. Retrieving the set of (τ_a, α) is more essential since the satellite-received radiance is not sensitive to the detailed structure of the size distribution but depends nearly uniquely on (τ_a, α).

In the present algorithm for simplicity we fix the vertical profile of the aerosol concentration, that is, the aerosol density is constant from 0- to 3-km height and is reduced lineally from 3- to 4-km height.

To calculate the phase function, single-scattering albedo, and the wavelength dependence of the aerosol optical thickness, we simply assume Mie particles with the size distribution in Eq. (10) and the complex refractive index of $m = 1.5 - 0.005i$. Introduction of the aerosol absorption is important for successful retrievals of the aerosol optical thickness (Ignatov et al. 1995a; Ignatov et al. 1995b; Nakajima and Higurashi 1997). The NOAA operational aerosol maps show that dust aerosols have the largest optical thickness contributing to the global atmospheric turbidity. The averaged imaginary index of refraction of dust aerosols is in a range from 0.003 to 0.005 for shortwave spectral region (Patterson and Gillette 1977; Carlson and Benjamin 1980). Urban-type aerosols also tend to have a large absorption (WCP 1983; Shettle and Fenn 1979; Tanaka et al. 1983; Hayasaka et al. 1992). The averaged value of imaginary index of refraction is in a range from 0.005 to 0.01. Ohta et al. (1996) measured the imaginary index of aerosols in the free atmosphere as 0.005 to 0.01 at the top of Mt. Lemmon, Arizona. Although we fix the aerosol complex refractive index as $1.5 - 0.005i$ in our algorithm, next generation algorithms can adopt more

sophisticated algorithms for an automatic determination of aerosol types with recent and near-future multichannel radiometers such as SeaWiFS, ADEOS/OCTS, and EOS-AMI/MODIS (Gordon et al. 1994; Fukushima and Toratani 1997; Kaufman and Tanré 1994).

c. *Application to the remote sensing of AVHRR*

For analyzing radiances in the visible and near-infrared channels of AVHRR, we have to take into account the gaseous absorption by ozone, oxygen, and water vapor with a specific spatial and temporal distribution, especially for ozone and water vapor. Extensive numerical simulations have shown that the effect of gaseous absorption on the AVHRR-received radiances can be approximated by correction factors for ozone absorption t_{O_3} and water vapor t_{H_2O} as

$$R = t_{O_3} t_{H_2O} R', \tag{12}$$

where R' is the reflectance with the gaseous absorption by other than ozone and water vapor, which are fixed with U.S. standard model in Air Force Geophysics Laboratory Lowtran-7. Here, t_{O_3} is given by

$$t_{O_3} = \exp[-\tau_{O_3}(1/\mu + 1/\mu_0)]. \tag{13}$$

The formula (13) is understandable, since ozone exists in the upper atmosphere, and a simple correction with two-way transmittance will be enough.

The correction for the water vapor absorption is more complicated. In our algorithm, we have tabulated the value of t_{H_2O} as the ratio of the apparent reflectance with water vapor to that without water vapor for eight solar zenith angles [θ_0 = 0° (10°) 70°], six satellite zenith angles [θ = 0° (10°) 50°], seven relative azimuth angles [ϕ = 0° (30°) 180°], eight cases for τ_a (1.0×10^{-10}, 0.001, 0.01, 0.02, 0.1, 0.4, 1, 2), and 10 cases for water vapor amount (w = 0, 0.04, 0.1, 0.2, 0.4, 1, 2, 4, 6, 10). In the calculations we have applied a Lowtran-type wavelength integration over the width of the response function of AVHRR with 15 wavelength grids for channel 1 and 22 grids for channel 2 that are set respectively for suitable evaluation of the water vapor and oxygen band absorption. The aerosol size distribution is fixed at γ = 1, since the size distribution effect is not significant in the results.

d. *Construction of LUT*

The coefficients in Eq. (9) depend on the geometry, that is, θ_0, θ, and ϕ, the aerosol optical property γ, and surface wind velocity u_{10}. Figure 4 shows relative errors in the apparent reflectances at TOA when the dependence on the wind velocity is ignored in calculating Eq. (9) other than the term R_s for various geometries. We have assumed the wind velocity at 10 m above the sea surface as u_{10} = 7 m s^{-1} to calculate the multiple component in synthesizing the TOA reflectance for various conditions (u_{10} = 1, 2, 7, 10, 15 m s^{-1}). According to

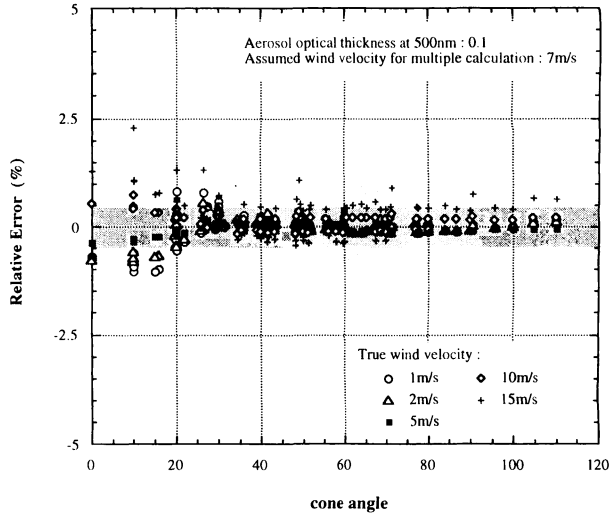

FIG. 4. Relative errors in the apparent reflectance at TOA synthesized with the multiple-scattering components ignoring the dependence of the wind velocity, that is, u_{10} = 7 m s^{-1}, for various geometries $0 < \theta_0 < 70$, $0 < \theta < 45$, $0 < \phi < 180$. Wind velocities for exact calculations are for u_{10} = 1, 2, 5, 10, and 15 m s^{-1}.

Fig. 4, the dependence of the TOA apparent reflectance on the wind velocity is mainly caused by the single-scattering component.

We therefore assume u_{10} = 7 m s^{-1} for constructing the LUT, which includes the coefficients in Eq. (9) for 29 solar zenith angles [θ_0 = 0° (2.5°) 70°], 21 satellite zenith angles [θ = 0° (2.5°) 50°], 23 relative azimuthal angles [ϕ = 0° (5°) 40°; 40° (10°) 180°], and 11 cases of the peak ratio (γ = 0.1, 0.2, 0.5, 1, 2, 3, 5, 10, 20, 50, 100). Figure 5 shows errors in R by approximation of Eq. (9) and interpolation for geometries on the whole sky at θ_0 = 60°. The figure shows the maximum error is less than 0.0007 except for the sun-glint region.

The water-leaving radiance has a strong dependence on wavelength and is very sensitive to the pigment concentration in the region of weak absorption of water. In other spectral regions, the radiance is almost unaffected by the pigment concentration in case 1 water (Gordon and Clark 1981), whereas the upwelling radiance from the ocean body is not small in case 2 water. We ignore this upwelling radiance in this study because more than 98% of the world ocean waters are presumably composed of case 1 water. The effect of scattering by foam in whitecap and water body becomes large as the surface wind velocity increases. We avoid data from analyses that u_{10} is greater than 15 m s^{-1} to avoid the foam effect.

3. Retrieval algorithm

Our algorithm for aerosol retrieval is based on an LUT approach. Measured radiances in channels 1 and 2 of AVHRR are compared with theoretical values that are reconstructed from LUT for trial values of aerosol parameters.

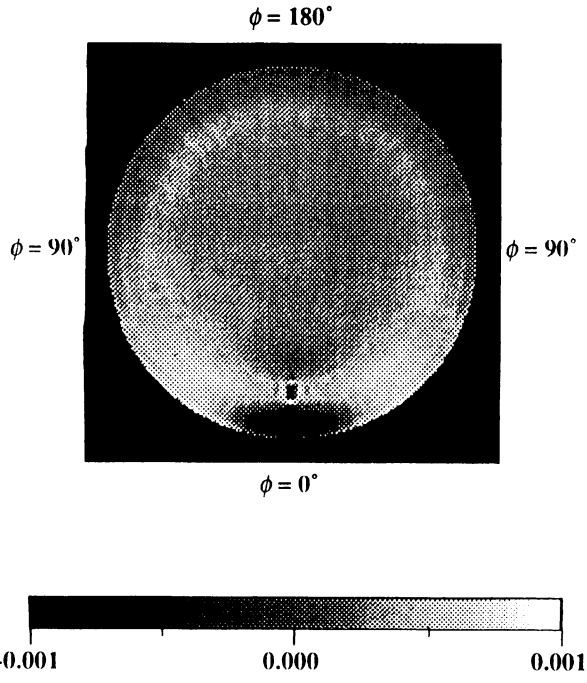

FIG. 5. The angular distribution of absolute errors in the apparent reflectance caused by the approximation Eq. (9) and angular interpolations at $\theta_0 = 60°$.

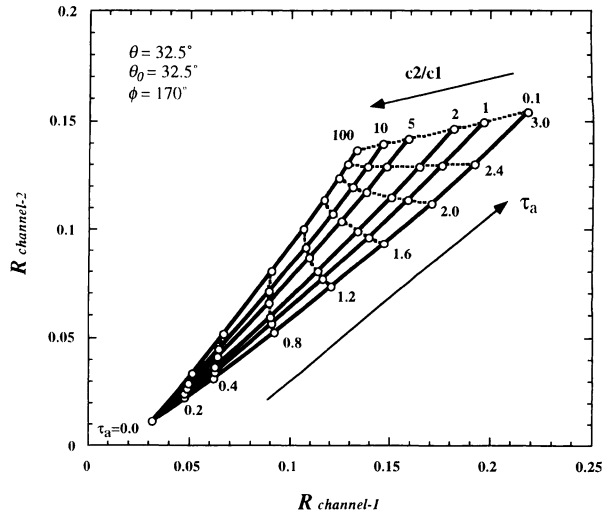

FIG. 6. The relationship between apparent reflectances of NOAA/AVHRR channels 1 and 2 for various aerosol loading conditions. τ_a = 0, 0.2, 0.4, 0.8, 1.2, 1.6, 2.0, 2.4, and 3.0; γ = 0.1, 1, 2, 5, 10, and 100; $\theta_0 = 32.5°$, $\theta = 32.5°$, and $\phi = 170°$.

a. *Retrievals of aerosol optical parameters*

The basis of retrieval is the characteristic relationship between apparent reflectances of AVHRR channels 1 and 2 for various values of the aerosol optical thickness at 0.5 μm τ_a and the peak ratio γ of the size distribution as shown in Fig. 6, which is caused by the difference in the extinction efficiency in each channel. The figure suggests that the aerosol optical parameters, that is, τ_a and γ, are retrieved by comparing measured reflectances and theoretical reflectances, which are obtained from LUT. In the sun-glint region, however, it is difficult to retrieve the aerosol optical parameters by this principle, since the relationship between two channel reflectances becomes complicated due to increasing contribution of directly reflected radiation by ocean surface (Nakajima and Higurashi 1997).

Differences between reflectances in channel 1 for τ_a = 0.0 and 0.1 are shown in Fig. 7 as a function of cone angles Θ', which are defined as the angle between the direction of specular reflection and the viewing direction,

$$\cos\Theta' = -\mu\mu_0 + \sqrt{1-\mu^2}\sqrt{1-\mu_0^2}\cos\phi. \quad (14)$$

In the figure, table values are assumed for θ_0, θ, and ϕ; u_{10} = 7 m s^{-1} and γ = 1. As explained above, the reflectance decreases with increasing optical thickness for $\Theta' < 20°$. It should be noted that a large increase of reflectance appears at $20° < \Theta' < 60°$, indicating that the optical thickness can be effectively retrieved in this cone angle range. The sensitivity decreases with further increases in cone angle, indicating that the optical thickness retrieval becomes difficult for large cone angles. An increase in the multiple-scattering contribution is not significant for large emergent zenith angles. We regard the region in which $\Theta' < 25°$ as the sun-glint region, and data in this region are excluded from the retrieval. Although we fixed 25° for all our analyses in this paper, data avoiding in the region of $\Theta' < 40°$ may be better for thin atmosphere cases and for taking into account the error in assumed wind velocity.

Reflectances in channels 1 and 2 of AVHRR outside the sun-glint region are compared with theoretical values that are reconstructed from LUT for trial values of τ_a and γ. The optimal values of τ_a and γ, which minimize the root-mean-square deviation ε between observed and theoretical reflectances, are searched by an iteration method until ε becomes less than 0.0001 for each channel and each grid value of γ. If we could not get the accuracy after 20 iterations, the data were discarded from the analysis. The peak ratio is then determined so that two values of τ_a estimated from channels 1 and 2 agree with each other.

b. *The accuracy of the retrieval*

We examine in Figs. 8 and 9 errors in retrieved values of the aerosol optical thickness and the Ångström exponent caused by the retrieval algorithm using numerical experiments. In these experiments, we assume table values at a grid point as test reflectance data and evaluate errors caused only by the inversion process. Other parameters assumed are w = 4.0 g cm^{-2} and u_{10} = 7 m s^{-1}. Figure 8 shows that the retrieval error in τ_a is less

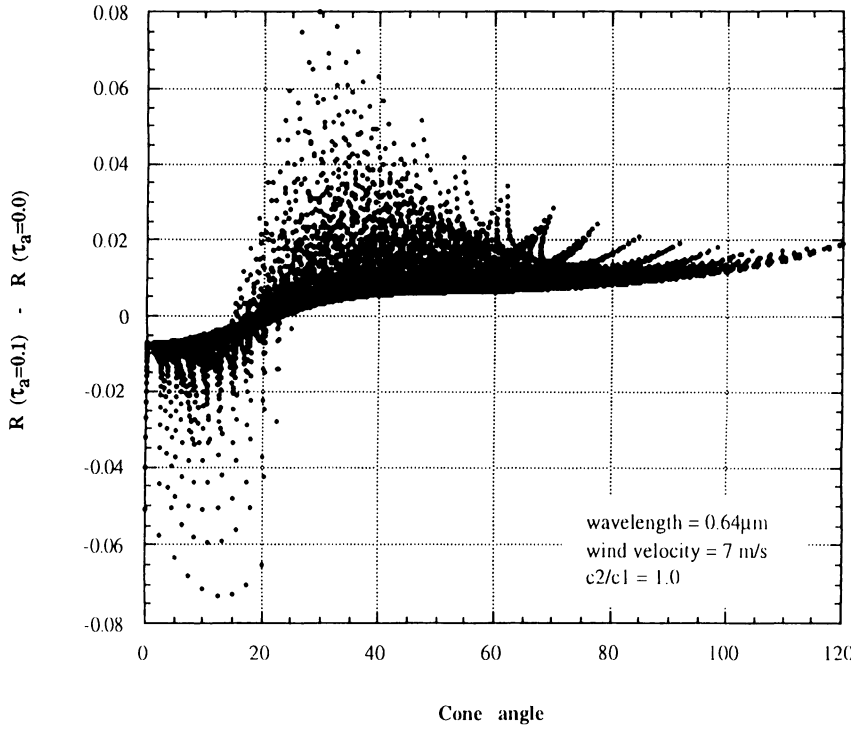

FIG. 7. Increases of the apparent reflectance with increasing optical thickness as a function of the cone angle. Values for various angular conditions are shown simultaneously.

than ±0.01 in most regions. Although the accuracy for optically thin cases seems to be better than thick cases in Fig. 8, various errors in obtaining the reflectance will cause a large retrieval error as understood by the shape of the small optical thickness region in Fig. 6. Figure 9 shows that the retrieval error in α is less than ±0.05 except for small cone angles and becomes worse as the optical thickness decreases due to the same reason as for optical thickness retrieval. It is more difficult to keep the accuracy of Ångström exponent retrieval than to keep the accuracy of optical thickness retrieval, because small differences of reflectances in channels 1 and 2 significantly affect the retrieval.

From the above experiments, it may be concluded that we have to be careful to retrieve aerosol optical thickness and Ångström exponent of thin aerosol layers. Along with interpolation errors of LUT by Eq. (9) and gas absorption correction errors by Eq. (12), the Ångström exponent retrieval can be affected by errors involved in the assumed water vapor amount, ozone amount, vertical profile of aerosol concentration, and calibration constants of the radiometer. Those errors are

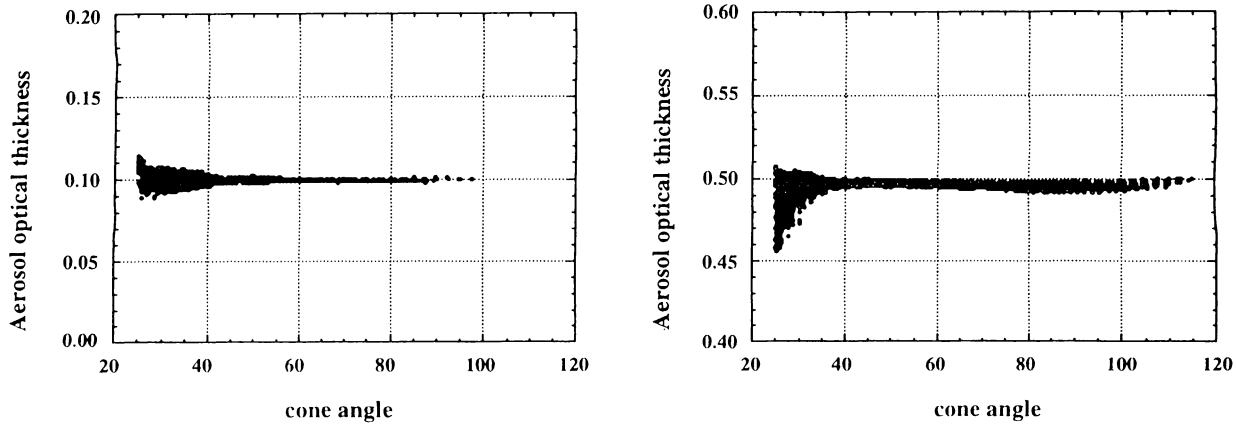

FIG. 8. The accuracy of retrieved aerosol optical thicknesses as a function of the cone angle. The true values are set as τ_a = 0.1 (left panel) and 0.5 (right panel) with α = 1.29.

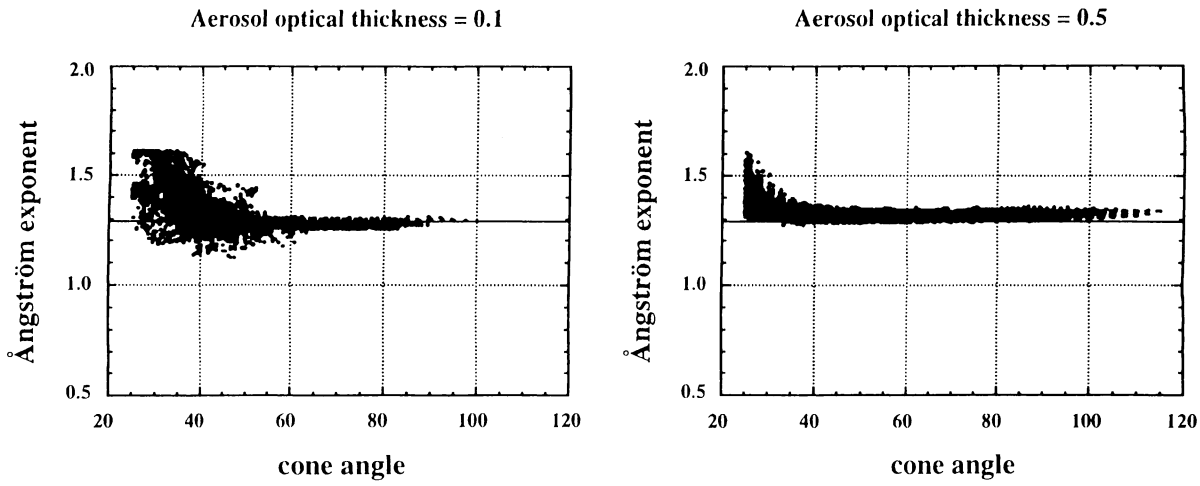

FIG. 9. The accuracy of retrieved Ångström exponents as a function of the cone angle. The true value is set as $\alpha = 1.29$ with $\tau_a = 0.1$ (left panel) and 0.5 (right panel).

expected to be wavelength dependent and hence cause an error in the Ångström exponent retrieval. For example, as studied in Higurashi et al. (1999, manuscript submitted to *Appl. Opt.*) the expected error in the Ångström exponent is less than 0.2 for an error in the assumed water vapor amount 2 g cm^{-2} for $\tau_a > 0.1$. As for the effect of an error in the assumed vertical aerosol concentration profile, numerical tests with two aerosol profiles, in which the aerosol layers are located at 0–4 km and 0–7 km, show that retrieved Ångström parameters start having a difference for $\tau_a < 0.2$.

Neglect of upwelling radiance from the ocean will cause an underestimation of the Ångström exponent for very turbid ocean. According to numerical simulations, however, its effect is not significant to retrievals at the wavelengths of AVHRR channels 1 and 2 ($\lambda = 0.64$ and 0.83 μm) in a general range of pigments and sediments (0.01–1.0 mg m^{-3}). Whitecaps will bring an error in the optical thickness retrieval, but not significantly in the Ångström exponent retrieval, because the whitecap contribution is nearly independent of wavelength. A detailed discussion will appear in Higurashi et al. (1999, manuscript submitted to *Appl. Opt.*)

4. Global data analysis

a. Datasets

The present retrieval algorithm has been applied to *NOAA-9* AVHRR GAC data in January and July of 1988. To analyze global data efficiently without missing the global feature of aerosol characteristics, 1.5° gridded segment datasets of AVHRR radiances in the region were made from 60°N to 60°S. Each 1.5° by 1.5° segment includes 10 by 10 pixels. One clear sky pixel datum was selected out of 100 pixels through the following screening steps. 1) Avoid data in which $\theta > 45°$ and $\theta_0 > 70°$ and data with $u_{10} > 15$ m s^{-1} to avoid the effect of whitecaps and $\Theta' < 25°$ to exclude sun glint. 2) Screen out cloudy pixels above threshold values, that is, $R_1 > 0.45$ or the brightness temperature for channel-4 T_{BB} less than 275 K. 3) Judge the remaining pixels to be suitable if they consist of more than 40 pixels, the 30th reflectance of channel 1 from the lowest in remaining pixels is less than 0.2, and the standard deviation of reflections of remaining pixels is less than 0.02; 4) Select the third reflection of channel 1 from the lowest in the remaining pixels.

Our algorithm requires three ancillary data, that is, total ozone amount, total water vapor amount, and surface wind velocity. Those data were obtained from TOMS gridded ozone data provided by the National Aeronautics and Space Administration (NASA)/Goddard Ozone Processing Team, the European Centre for Medium-Range Weather Forecasts objective analysis data, and Special Sensor Microwave/Imager–derived data, which is produced by Robert Atlas and Joseph Ardizzone (NASA/Goddard Space Flight Center).

b. Sensor calibration

Since the visible channel sensors of AVHRR have been degrading from the prelaunch calibration, after the launch a correction is necessary to reduce the retrieval error due to a calibration error. There have been persistent efforts for monitoring the calibration constants as a function of time (e.g., Che and Price 1992; Holben et al. 1990; Kaufman and Holben 1993). Most investigators use the following transformation formula of digital counts to radiances:

$$L_i = \alpha_i(C_i - C_{0i}), \tag{15}$$

where L_i is the spectral radiance detected by the sensor in channel i, C_i is the digital count value on a data tape, α_i is the calibration coefficient, and C_{0i} is the deep space count for channel i. Kaufman and Holben (1993) have

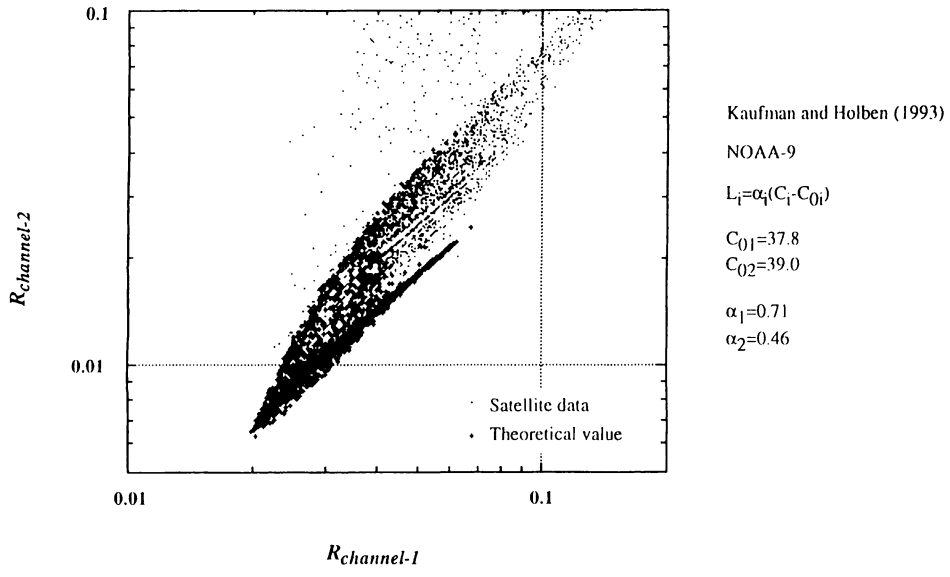

FIG. 10. The distribution of minimum radiances in 1.5° × 1.5° segments over globe. Circles show AVHRR data in channels 1 and 2, and dots show corresponding theoretical values without aerosol loading. Radiances are transformed from digital data by Eq. (15) with C_{01} = 37.8, C_{02} = 39.0, α_1 = 0.71, and α_2 = 0.46.

proposed C_{01} = 37.8, C_{02} = 39.0, α_1 = 0.71, and α_2 = 0.46 for January and July of 1988.

For aerosol remote sensing, especially for thin aerosol layer cases, sensor calibration is a serious problem, because a small error in radiances may cause a large error in retrieved results as indicated in Fig. 6. It is therefore desirable to investigate the validity of the assumed calibration constants for our retrieval scheme. Figure 10 plots the observed minimum reflections among clear sky pixels in each segment obtained with Kaufman and Holben's calibration constants against the theoretical minimum values that correspond to no aerosol loading cases for each segment. The figure shows that calibrated satellite radiances with Kaufman and Holben's calibration constants fall within the theoretical region as a whole, suggesting that the calibration constants can generate consistent values of reflectance with our optical model. It should be noted that small changes in the calibration constants from the assumed values will cause intolerable modifications of the data region from the shown pattern in Fig. 10. In other words, it will be possible to determine calibration constants very accurately from such a plot if we are provided with aerosol optical thickness and Ångström exponent for thin aerosol layers by ground-based measurements. Observed data points outside theoretical region have systematically larger reflectances in channel 2, indicating that those points had a cloud and/or whitecap contamination or other effects other than molecular scattering and surface reflection.

c. Results

The retrieval algorithms and calibration constants were applied to the AVHRR GAC data for 10 days of January and July 1988. A 10-day composite was made by taking a mean value of the results we could retrieve in 10 days for each segment. Figure 11 shows such 10-day composites of retrieved aerosol optical thicknesses in January and July 1988. Due to the restriction on the solar zenith angle $\theta_0 < 70°$ there were no retrievals in mid- and high latitudes of the winter hemisphere. We see in Fig. 11 that there are several specific regions of large optical thickness, off the west coast of North Africa, the Arabian Peninsula, and the west coast of southern Africa. Saharan dust particles form the largest aerosol layer, off the west coast of North Africa extending across the Atlantic Ocean along the trade winds. The tongue of the aerosol layer becomes dispersed, shifting to the south in January as compared with that in July. This seasonal change in aerosol loading pattern is consistent with the flow pattern of the surface wind fields used in retrievals as shown in Fig. 12. The aerosol layer off the west coast of southern Africa in July also can be explained by the wind field. Herman et al. (1997) has pointed out that these aerosols are caused by a biomass burning in the southern African region. Those features have been found by NOAA operational aerosol products (Stowe et al. 1997), but it should be noted that the mean optical thickness is twice as large as the NOAA values. This difference may be caused by differences in the two algorithms, that is, assumed size distribution, lower boundary condition for radiative transfer, and calibration constants. It is also possible that an inaccurate cloud screening might cause an overestimation of the retrieved aerosol optical thickness in the present study. We need more ground truth to establish the accuracy of retrieved values of optical thickness.

Figure 13 shows the distribution of the Ångström

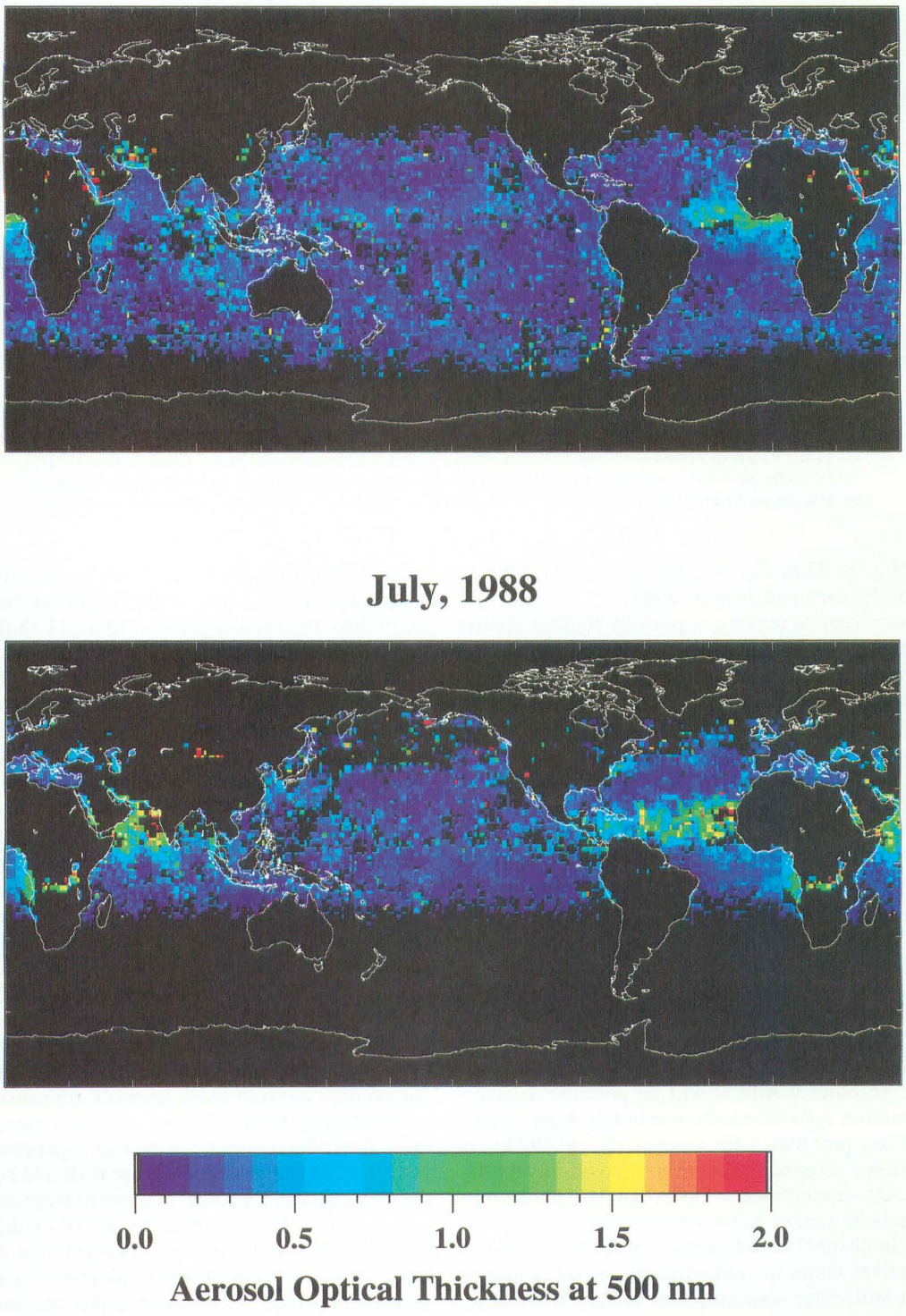

FIG. 11. The 10-day composite of retrieved aerosol optical thicknesses at 0.5 μm in January and July 1988.

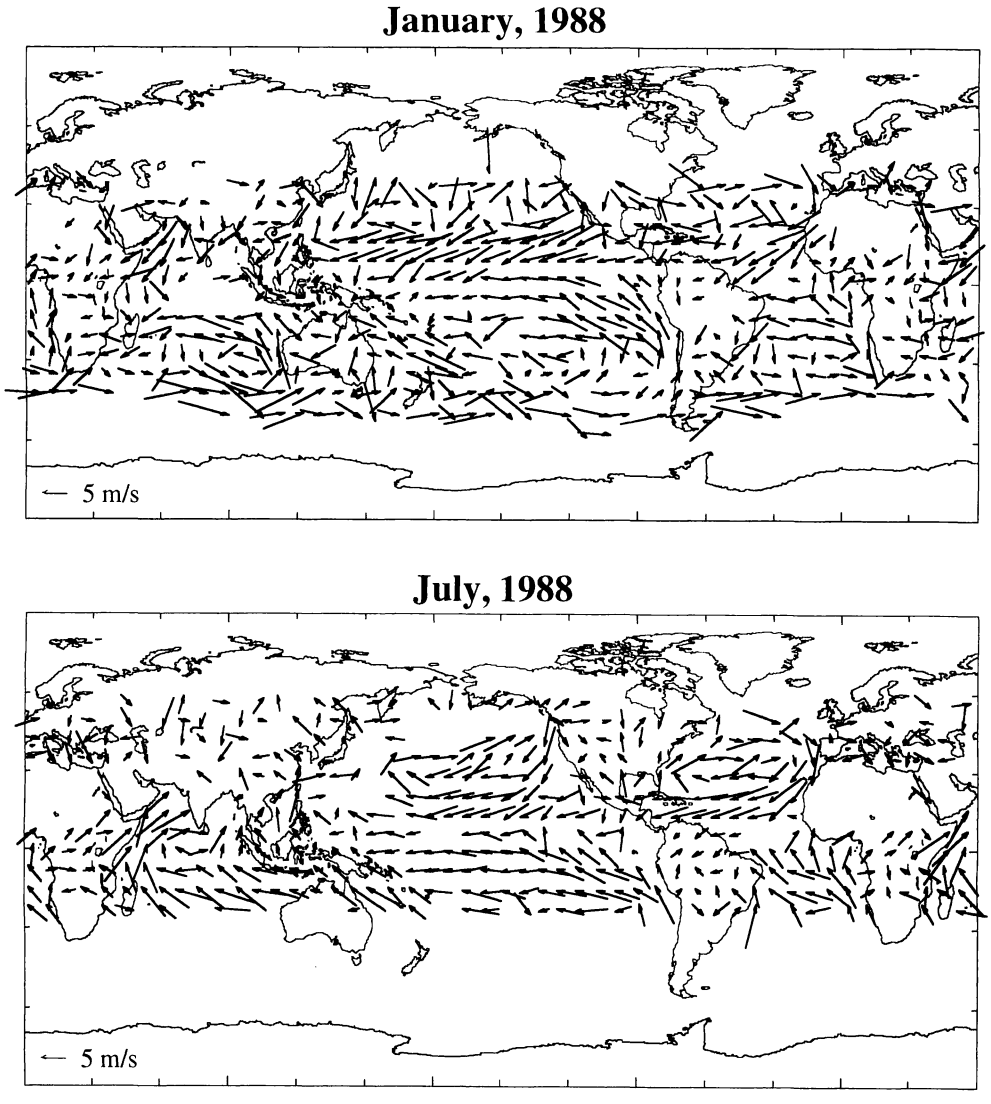

FIG. 12. Averaged surface wind velocities for the analyses shown in Fig. 11.

exponent corresponding to the retrieved optical thickness distribution shown in Fig. 12. Pixels with optical thickness less than 0.2 were masked, because retrieved Ångström exponents for thin optical thickness are uncertain, as discussed in section 3b. Ångström exponents for optically thick regions are about 0.5 off the west coast of North Africa and off the Arabian Peninsula and around 0.7 for the west coast of southern Africa. A remarkable feature in Fig. 13 is that there are large Ångström exponent regions in July around the Black Sea, off the east coast of North America around New York, and off the east coast of southern China around Shanghai. Since those regions correspond to the world's larger industrial areas, it is highly possible that large Ångström exponents in these regions were caused by small particles associated with anthropogenic pollutants. With a careful comparison of aerosol optical thickness maps with Ångström exponent maps for July we can recognize slight increases in the optical thickness in these regions. Over time will be possible by such comparison to evaluate the optical thickness increase due to anthropogenic aerosols.

5. Discussion and conclusions

We have obtained global distributions of aerosol optical thickness and Ångström exponent as our main results as shown in Figs. 11 and 13, applying the proposed algorithm to 10-day AVHRR GAC datasets. The spatial pattern of the optical thickness distribution is similar to the NOAA operational products, but the magnitude tends to be twice as large as NOAA products (Husar et al. 1997). As listed in the preceding section, there are significant differences between our algorithm and the

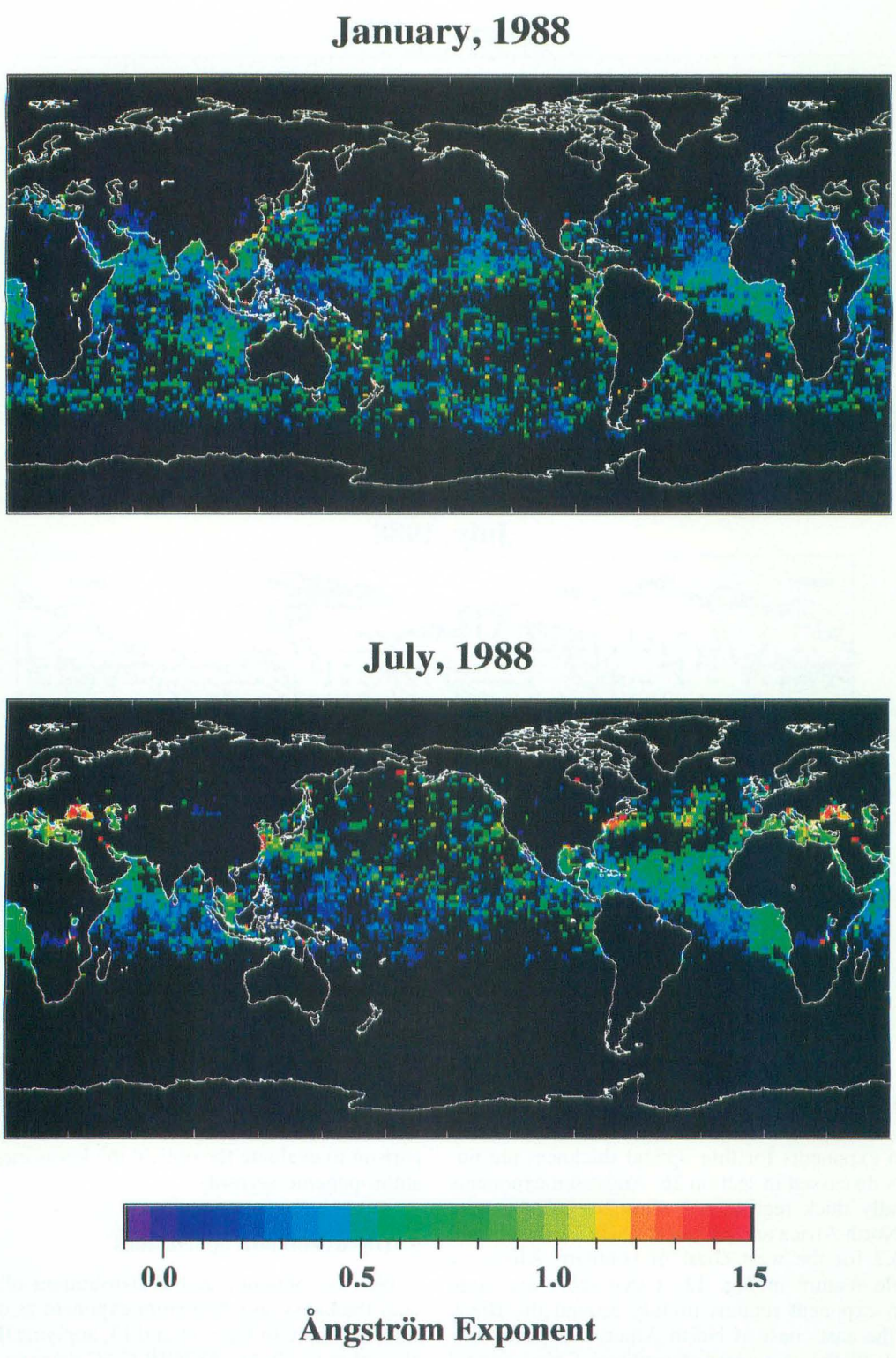

FIG. 13. The 10-day composite of retrieved Ångström exponents in January and July 1988.

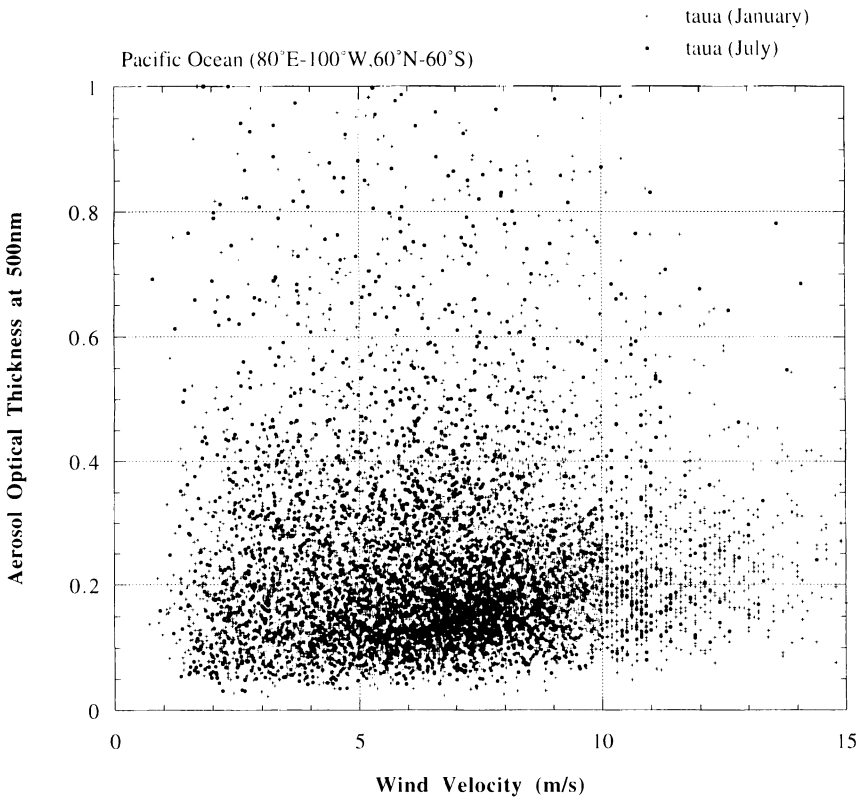

FIG. 14. Retrieved aerosol optical thicknesses plotted against the surface wind velocity in a Pacific Ocean area (80°E–100°W, 60°N–60°S).

NOAA operational algorithm, so that we have to be careful before drawing the final conclusions to the evaluation. There are some problems with our products as compared with NOAA products. Figure 11 shows an aerosol plume over the Arabian Sea extending to the southeast in the July case, whereas the wind flow direction is rather to the northeast. One possible explanation is a contamination by whitecaps generated by the strong wind in this season. To study this point, we plot in Fig. 14 the aerosol optical thickness against the surface wind velocity in a region from 80°E to 100°W and from 60°N to 60°S including the Pacific Ocean and the eastern Indian Sea. The figure shows that the minimum value of optical thickness for each wind velocity slightly increases with increasing wind velocity. This fact suggests that retrieved optical thicknesses may have contributions from whitecap and/or injected particles from roughened ocean. It should be noted, however, that this effect seems to be less than 0.1 in optical thickness for the wind velocity less than 15 m s^{-1} and is unlikely to be the reason for the large optical thickness around the region. We will need a future ground truth for understanding the feature.

In the above context it should be pointed out that a prescribed phase function may give a better value of the aerosol optical thickness when it is small, because various uncertainties in the assumptions for the retrieval can propagate to the optical thickness retrieval process through ill retrievals of Ångström exponent, as discussed in section 3b. It is therefore recommended that in the future we should develop an automatic switching algorithm between an adjusted Ångström exponent method, as in the present study, and a prescribed Ångström exponent method with a classification technique of aerosol types. At the same time, we have to accumulate more ground truth of the present method in order to study the limitation of the method.

To see the validity of the optical properties thus obtained, relationships between aerosol optical thickness and Ångström exponents are shown in Fig. 15 for six particular areas in July 1988, that is, the west coast of North Africa, the west coast of south Africa, the Black Sea, the Mediterranean Sea, the east coast of North America, and the east coast of southern China. Longitudes and latitudes of the regions are listed in Table 2. The figure shows that off the west coast of North Africa the Ångström exponent increases from about 0.3 to 0.5 with increasing optical thickness and is almost constant after reaching 0.5. In this region, the Ångström exponent stays at small values due to large desert dust particles.

For the region off the west coast of southern Africa, the Ångström exponent is larger in the range from 0.5 to 0.7, with the maximum at optical thickness around 0.5. If those aerosols are of biomass burning origin as

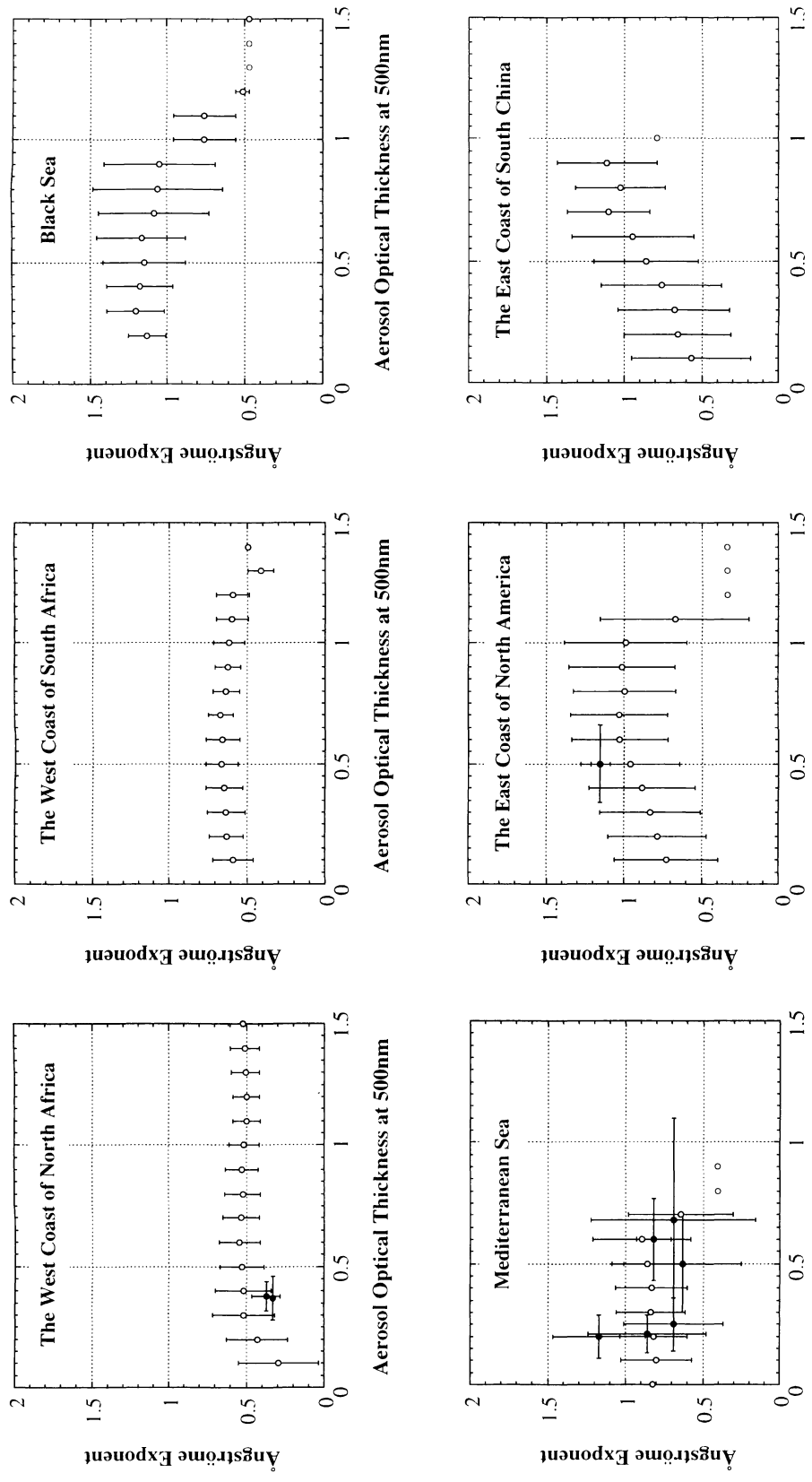

FIG. 15. Correlations between τ_a and α for six peculiar areas of the results in July 1988, that is, the west coast of North Africa, the west coast of south Africa, the Black Sea, the Mediterranean Sea, the east coast of North America, and the east coast of south China. Satellite-derived values (circles) and ground-based measurement values (dots) by several investigators listed in Table 3 are shown.

TABLE 2. Areas for analyses shown in Fig. 15.

Latitude	Longitude	Notes
25°N 10°N	40°W 10°W	off the west coast of North Africa
20°N 10°N	60°W 40°W	
10°N 15°S	0°E 15°E	off the west coast of southern Africa
50°N 40°N	25°E 45°E	Black Sea
50°N 30°N	0°E 25°E	Mediterranean Sea
40°N 30°N	25°E 30°E	
45°N 35°N	80°W 60°W	off the east coast of North America
35°N 25°N	120°E 125°E	off the east coast of southern China

Herman et al. (1997) suggested, the value of the Ångström exponent is expected to be a rather small with a bimodal feature of the aerosol size distribution with both the accumulation and smoldering mode aerosols (Holben et al. 1999, manuscript submitted to *Remote Sens. Environ.*). It is also possible that there is a contribution from soil particles originating from the Kalahari desert. Therefore, the characteristic dependence of the Ångström exponent on the aerosol optical thickness is caused by a correlation between the accumulation mode and the large coarse particle mode attributed to soil or ash particles.

In the regions on the Black Sea, the regions off the east coast of North America, and the regions off the east coast of South China, which are expected to be affected by anthropogenic pollutants, the Ångström exponent tends to increase with increasing τ_a until α reaches around 1 and then decreases as τ_a increases further. This characteristic dependence of α on τ_a was also found with in situ measurement data for urban-type atmospheres (Kaufman et al. 1996). The first increase of α corresponds to an increasing contribution of accumulation mode particles relative to the contribution from background aerosols. The decrease of α with further increase in optical thickness can be caused by particle growth due to water vapor uptake.

In Fig. 15 and Table 3 we introduce ground truth data from several investigators. Our results agree with the ground-based measurements within the tolerance of uncertainties and errors associated with various measurement techniques. For the Mediterranean Sea, however, the agreement looks poor. In this region there are several aerosol sources with quite different Ångström exponents, that is, Saharan desert dust, maritime particles, and urban aerosols from Europe, so that the Ångström exponent value may change significantly and may be difficult to be validated.

To our knowledge, the only previous retrieval of the global distribution of an aerosol size parameter is that of Durkee et al. (1991). It is very interesting to compare our result with theirs. They found that the aerosol optical thickness and size parameter show marked differences between the Northern and Southern Hemispheres. They suggested this feature is consistent with Northern Hemispheric continental sources of small particles. It is difficult to see a similar phenomenon in our results. Durkee et al. also claimed that they have detected small DMS aerosols around the equator, whereas our results do not show such small aerosol particles in the region. Such differences in the two studies may be attributed to differences in the observation time. It should be noted, however, that there might be some effect from water vapor in the result of Durkee et al., since the water vapor correction of channel-2 radiance is very difficult and delicate. A significant discontinuity in their retrieval results at edges of scan lines shows some problems in their interpretation of the satellite-received radiances. We need a ground truth to explain these differences.

Although there are several unsolved problems as mentioned above, it is found that our lookup table method with NOAA AVHRR channel-1 and -2 radiances is sufficiently useful to depict global distributions of different aerosol types through aerosol optical thickness and Ångström exponent. The obtained distributions show that the majority of atmospheric aerosols originate from desert dust, biomass burning, and human activities. Particularly, the loading of desert dust particles are conspicuously strong, and its impacts extend broadly by long distance atmospheric transport. Although anthropogenic aerosols do not strongly contribute to the atmospheric turbidity as compared with desert dust, they can be clearly identified with the Ångström exponent with significantly large values exceeding 1.0.

In the future, we have to estimate more detailed optical parameters, such as mode radii of the size distribution, composition, etc., using multichannel radiance data from advanced radiometers, such as ADEOS/OCTS, EOS-AM1/MODIS, and ADEOS2/GLI.

TABLE 3. Aerosol optical thicknesses (τ_a) at 0.5 μm and Ångström exponents (α) measured by several investigators for comparison with Fig. 15. Here, σ and σ_α are root-mean-square deviations of measured τ_a and α.

Reference	Period of time	τ_a	σ	α	σ_α	Area
Villevalde et al. (1984)	17 July 1983–30 July 1983	0.50	0.20	0.63	0.38	Mediterranean Sea
Shifrin et al. (1989)	4 June 1983–17 June 1983	0.25	0.11	0.69	0.32	Mediterranean Sea
Deuze et al. (1988)	20 July 1983–29 July 1983	0.68	0.42	0.69	0.53	Mediterranean Sea
Volgin et al. (1988)	11 August 1986–16 September 1986	0.20	0.09	1.17	0.30	Mediterranean Sea
Zibordi et al. (1988)	28 May 1983–1 June 1983	0.60	0.17	0.82	0.11	Mediterranean Sea
Yershov et al. (1990)	25 June 1988–22 July 1988	0.21	0.08	0.86	0.38	Mediterranean Sea
Reddy et al. (1990)	6 May 1988–12 May 1988	0.37	0.09	0.33		Saharan dust
	30 August 1988–31 August 1988	0.38	0.06	0.37	0.09	Saharan dust
	16 July 1988–4 August 1988	0.50	0.16	1.15	0.06	North American air

Acknowledgments. J. Tucker of GSFC and ARGASS (AVHRRGAC dataset for Atmosphere and Surface Studies) Project, led by R. Imasu of NIRE, is appreciated for providing us with AVHRR-GAC data used in this study. The ancillary data used in this study for ozone amount are provided by Ms. Patricia T. Guimaraes, Dr. Richard D. Mcpeters, Dr. Arlin J. Krueger/NASA GSFC, members of the TOMS NIMBUS Experiment and Ozone Processing Teams and the National Space Science Data Center, and for surface wind velocity by Dr. R. Atlas and Dr. S. C. Bloom. This paper is the result of three research projects supported by the Research Fellowships of the Japan Society for the Promotion of Science for Young Scientists, the Grant-in-Aid for Scientific Research on Priority Areas (No. 08241104) of the Japanese Ministry of Education, Science, Sports and Culture, and OCTS/GLI projects of the National Space Development Agency of Japan. The content of this paper has been submitted for a Ph.D. dissertation by A. Higurashi to the University of Tokyo.

REFERENCES

Atlas, R., and S. C. Bloom, 1989: Global surface-wind vectors resulting from the assimilation of satellite wind-speed data in atmospheric general circulation models. *Proc. OCEANS '89* 260–265.

——, ——, R. N. Hoffman, J. V. Ardizzone, and G. Brin, 1991: Space-based surface-wind vectors to aid understanding of air–sea interactions. *Eos, Trans. Amer. Geophys. Union*, **72,** 18.

Carlson, T. N., and S. G. Benjamin, 1980: Radiative heating rates for Saharan dust. *J. Atmos. Sci.*, **37,** 193–213.

Chandrasekhar, S., 1960: *Radiative Transfer.* Dover, 393 pp.

Charlson, R. J., S. E. Schwartz, J. M. Hales, R. D. Cess, J. A. Coakley Jr., J. E. Hansen, and D. J. Hofmann, 1992: Climate forcing by anthropogenic aerosols. *Science*, **255,** 423–430.

Deuze, J. L., C. Devaux, M. Herman, R. Santer, and D. Tanré, 1988: Saharan aerosols over the South of France: Characterization derived from satellite data and ground based measurements. *J. Appl. Meteor.*, **27,** 680–686.

Durkee, P. A., F. Pfeil, E. Frost, and R. Shema, 1991: Global analysis of aerosol particle characteristics. *Atmos. Environ.*, **25A,** 2457–2471.

Fukushima, H., and M. Toratani, 1997: Asian dust aerosol: Optical effect on satellite ocean color signal and a scheme of its correction. *J. Geophys. Res.*, **102** (D14), 17 119–17 130.

Gordon, H. R., and D. K. Clark, 1981: Clear water radiances for atmospheric correction of coastal zone color scanner imagery. *Appl. Opt.*, **24,** 4175–4180.

——, and M. Wang, 1992: Surface-roughness considerations for atmospheric correction of ocean color sensors. I: The Rayleigh-scattering component. *Appl. Opt.*, **31,** 4261–4267.

——, and ——, 1994: Retrieval of water-leaving radiance and aerosol optical thickness over the oceans with SeaWiFS: A preliminary algorithm. *Appl. Opt.*, **33,** 443–452.

Hansen, J. E., and A. A. Lacis, 1990: Sun and dust versus greenhouse gases: An assessment of their relative roles in global climate change. *Nature*, **346,** 713–719.

Hayasaka, T., T. Nakajima, S. Ohta, and M. Tanaka, 1992: Optical and chemical properties of urban aerosols in Sendai and Sapporo, Japan. *Atmos. Environ.*, **26A,** 2055–2062.

Herman, J. R., P. K. Bhartia, O. Torres, C. Hsu, C. Seftor, and E. Celarier, 1997: Global distribution of UV-absorbing aerosols from Nimbus 7/TOMS data. *J. Geophys. Res.*, **102,** (D14), 16 911–16 922.

Higurashi, A., T. Nakajima, and T. Tanaka, 1999: A study on synthesizing satellite-received radiances for aerosol and ocean color remote sensing. *Appl. Opt.*, in press.

Holben, B. N., and Coauthors, 1999: Automatic sun and sky scanning radiometer system for network aerosol monitoring. *Remote Sens. Environ.*, in press.

Husar, R. B., J. M. Prospero, and L. L. Stowe, 1997: Characterization of tropospheric aerosols over the oceans with the NOAA advanced very high resolution radiometer optical thickness operational product. *J. Geophys. Res.*, **102,** 16 899–16 909.

Ignatov, A. M., L. L. Stowe, S. M. Sakerin, and G. Korotaev, 1995a: Validation of NOAA/NESDIS satellite aerosol product over the North Atlantic in 1989. *J. Geophys. Res.*, **100,** 5123–5132.

——, ——, R. Singh, S. Sakerin, D. Kabanov, and I. Dergileva, 1995b: Validation of NOAA/AVHRR aerosol retrievals using sun-photometer measurements from R/V AKADEMIK VERNADSKY in 1991. *Adv. Space Res.*, **16,** 95–98.

Jones, A., D. L. Roberts, and A. Slingo, 1994: A climate model study of indirect radiative forcing by anthropogenic sulfate aerosols. *Nature*, **370,** 450–453.

Junge, C. E., 1969: Comments on "Concentration and size distribution measurements of atmospheric aerosols and a test of the theory of self-preserving size distributions." *J. Atmos. Sci.*, **26,** 603–608.

Kaufman, Y. J., and B. N. Holben, 1993: Calibration of the AVHRR visible and near-IR bands by atmospheric scattering, ocean glint and desert reflection. *Int. J. Remote Sens.*, **14,** 21–52.

——, and T. Nakajima, 1993: Effect of Amazon smoke on cloud microphysics and albedo-analysis from satellite imagery. *J. Appl. Meteor.*, **32,** 729–744.

——, and D. Tanré, 1994: Algorithm for remote sensing of tropospheric aerosol from MODIS: Optical thickness over land and ocean and aerosol size distribution over the ocean. MODIS ATBD.

——, and B. N. Holben, 1996: Hemispherical backscattering by biomass burning and sulfate particles derived from sky measurements. *J. Geophys. Res.*, **101,** 19 433–19 445.

——, R. S. Fraser, and R. A. Ferrare, 1990: Satellite measurements of large-scale air pollution: Methods. *J. Geophys. Res.*, **95,** 9895–9909.

——, A. Gitelson, A. Karnieli, E. Ganor, R. S. Fraser, T. Nakajima, S. Mattoo, and B. N. Holben, 1994: Size distribution and scattering phase function of aerosol particles retrieved from sky brightness measurements. *J. Geophys. Res.*, **99,** 10 341–10 356.

Kiehl, J. T., and B. P. Briegleb, 1993: The relative roles of sulfate aerosols and greenhouse gases in climate forcing. *Science*, **260,** 311–314.

Kneizys, F. X., E. P. Shettle, L. W. Abreu, J. H. Chetwynd, G. P. Anderson, W. O. Gallery, J. E. A. Selby, and S. A. Clough, 1988: User's Guide to LOWTRAN 7. Rep. AFGL-TR-88-0177.

Koepke, P., 1984: Effective reflectance of oceanic whitecaps. *Appl. Opt.*, **23,** 1816–1824.

Kondratyev, K. Ya., R. M. Welch, S. K. Cox, V. S. Grishechkin, V. A. Ivanov, M. A. Prokofyev, V. F. Zhvalev, and O. B. Vasilyev, 1981: Determination of vertical profiles of aerosol size spectra from aircraft radiative flux measurements. Pt. 1. Retrieval of spherical particle size distribution. *J. Geophys. Res.*, **86,** 9783–9793.

Li, X., H. Maring, D. Savoie, K. Voss, and J. M. Prospero, 1996: Dominance of mineral dust in aerosol light-scattering in the North Atlantic trade winds. *Nature*, **380,** 416–419.

Nakajima, T., and M. Tanaka, 1983: Effect of wind-generated waves on the transfer of solar radiation in the atmosphere-ocean system. *J. Quant. Spectrosc. Radiat. Transfer*, **29,** 521–537.

——, and ——, 1986: Matrix formulations for the transfer of solar radiation in a plane-parallel scattering atmosphere. *J. Quant. Spectrosc. Radiat. Transfer*, **35,** 13–21.

——, and ——, 1988: Algorithms for radiative intensity calculations in moderately thick atmospheres using a truncation approximation. *J. Quant. Spectrosc. Radiat. Transfer*, **40,** 51–69.

——, and H. Fukushima, 1996: Development of radiance tables for aerosol remote sensing (in Japanese). Annual Rep. for the OCTS Sensor Team in 1996, National Space Development Agency of Japan.

——, and A. Higurashi, 1997: AVHRR remote sensing of aerosol optical properties in the Persian Gulf region, the Summer of 1991. *J. Geophys. Res.*, **102** (D14), 16 935–16 946.

——, M. Tanaka, M. Yamano, M. Shiobara, K. Arao, and Y. Nakanishi, 1989: Aerosol optical characteristics in the Yellow Sand events observed in May, 1982 in Nagasaki—Part II Models. *J. Meteor. Soc. Japan*, **67**, 279–291.

Ohta, S., M. Hori, N. Murao, S. Yamagata, and K. Gast, 1996: Chemical and optical properties of lower tropospheric aerosols measured at Mt. Lemmon in Arizona. *J. Global Environ. Eng.*, **2**, 67–78.

Patterson, E. M., and D. A. Gillette, 1977: Commonalities in measured size distributions for aerosols having a soil-derived component. *J. Geophys. Res.*, **82**, 2074–2082.

——, ——, and B. H. Stockton, 1977: Complex index of refraction between 300 and 700 nm for Saharan aerosols. *J. Geophys. Res.*, **82**, 3153–3160.

Reddy, P. L., F. W. Kreiner, J. J. DeLuisi, and Y. Kim, 1990: Aerosol optical depths over the Atlantic derived from shipboard sunphotometer observations during the 1988 global change expedition. *Global Biogeochem. Cycles*, **4**, 225–240.

Remer, L., S. Gasso, D. Hegg, Y. Kaufmann, and B. Holben, 1997: Urban/industrial aerosol: Ground-based sun/sky radiometer and airborne in situ measurements. *J. Geophys. Res.*, **102** (D14), 16 849–16 859.

Shettle, E. P., and R. W. Fenn, 1979: Models for the aerosols of the lower atmosphere and the effects of humidity variations on their optical properties. AFGL-TR-79-0214.

Shi, G. Y., J. D. Guo, X. B. Fan, B. Wang, and L. X. Wang, 1994: Climate change and its causes. *Proc. Int. Conf. on Regional Environment and Climate Change in East Asia.*

Shifrin, K. S., V. M. Volgin, B. N. Volkov, O. A. Yershov, and A. V. Smirnov, 1989: Optical depth of atmospheric aerosol over the sea. *Sov. J. Remote Sens.*, **5** (4), 591–605.

Shiobara, M., T. Hayasaka, T. Nakajima, and M. Tanaka, 1991: Aerosol monitoring by use of a scanning spectral radiometer in Sendai, Japan. *J. Meteor. Soc. Japan*, **69**, 57–70.

Smirnov, A., O. Yershov, and Y. Villevalde, 1995: Measurement of aerosol optical depth in the Atlantic Ocean and Mediterranean Sea. *Proc. EUROPTO*, Paris, France, SPIE, 27–28.

Stowe, L. L., R. M. Carey, and P. P. Pellegrino, 1992: Monitoring the Mt. Pinatubo aerosol layer with NOAA/11 AVHRR data. *Geophys. Res. Lett.*, **19**, 159–162.

Tanaka, M., T. Takamura, and T. Nakajima, 1983: Refractive index and size distribution of aerosols as estimated from light scattering measurements. *J. Climate Appl. Meteor.*, **22**, 1253–1261.

Taylor, K. E., and J. E. Penner, 1994: Response of the climate system to atmospheric aerosols and greenhouse gases. *Nature*, **369**, 734–737.

Tegen, I., A. A. Lacis, and I. Fung, 1996: The influence on climate forcing of mineral aerosols from disturbed soils. *Nature*, **380**, 419–422.

Toon, O. B., and J. B. Pollack, 1976: A global average model of atmospheric aerosols for radiative transfer calculations. *J. Appl. Meteor.*, **15**, 225–246.

Twomey, S., 1977: The influence of pollution on the shortwave albedo of clouds. *J. Atmos. Sci.*, **34**, 1149–1152.

Villevalde, Y. V., K. S. Lamden, and A. V. Smirnov, 1984: The results of maritime, atmospheric spectral transmittance measurements (in Russian). *Extended Abstracts, Eighth All-Union Symposium on Laser and Acoustic Soundings of the Atmosphere, Part 1*, Tomsk, USSR, Institute of Atmospheric Optics, 111–113.

Volgin, V. M., O. A. Yershov, A. V. Smirnov, and K. S. Shifrin, 1988: Optical depth of aerosol in typical sea areas. *Izv. Acad. Sci. USSR, Atmos. Oceanic Phys.*, **24**, 272–277.

Wang, M., and H. R. Gordon, 1993: Retrieval of the columnar aerosol phase function and single-scattering albedo from sky radiance over the ocean: Simulations. *Appl. Opt.*, **32**, 4598–4609.

WCP, 1983: Report of the experts meeting on aerosols and their climatic effects. WMO-ICSU WCP-55.

Whitby, K. T., 1978: The physical characteristics of sulfur aerosols. *Atmos. Environ.*, **12**, 135–159.

Yershov, O. A., A. V. Smirnov, and K. S. Shifrin, 1990: Spectral transparency and solar halo in the atmosphere above the ocean (English translation). *Izv. Acad. Sci. USSR, Atmos. Oceanic Phys.*, **26**, 287–292.

Zibordi, G., and G. Maracci, 1988: Determination of atmospheric turbidity from remotely-sensed data: A case study. *Int. J. Remote Sens.*, **9**, 1881–1894.